A CONTINUOUS APPROACH TO DISCRETE ORDERING ON $\mathbb{S}^2$*

RAINER BACKOFEN†, MANUEL GRÄF‡, DANIEL POTTS§, SIMON PRAETORIUS¶, AXEL VOIGT‖, AND THOMAS WITKOWSKI**

Abstract. We consider the classical problem to find optimal distributions of interacting particles on a sphere by solving an evolution problem for a particle density. Starting from a given pair potential we sketch the derivation of the resulting higher order surface partial differential equation, which is an approximation of a surface dynamic density functional theory. Different numerical approaches are discussed to solve the evolution problem: (a) an implicit approach to describe the surface using a phase-field description, (b) a parametric finite element approach, and (c) a spectral method based on nonequispaced fast Fourier transforms on the sphere. Results for computed minimal energy configurations are discussed for various particle numbers and extensions to other more complex and evolving surfaces are mentioned

Key words. ordering on curved surfaces, Thomson problem, dynamic density functional theory, phase field crystal, PDE on surfaces

AMS subject classifications. 35R01, 35K25, 42C10

1. Introduction.

The centennial of Hilbert's announcement of his mathematical problems for the 20th century was the natural occasion to propose a "new set of Hilbert problems". One of these problems proposed by Smale [1] ask about the distribution of N points on a sphere. Let

$$V_N(\mathbf{r}) = \sum_{1\le i<j\le N} 1/\|\mathbf{r}_i - \mathbf{r}_j\|^\beta, \quad \text{and} \quad V_N = \min_{\mathbf{r}} V_N(\mathbf{r})$$

with $\mathbf{r} = (\mathbf{r}_1, \ldots, \mathbf{r}_N)$, $\mathbf{r}_i$ distinct points on the 2-sphere $\mathbb{S}^2$, $\|\mathbf{r}_i - \mathbf{r}_j\|$ the distance in $\mathbb{R}^3$ and $\beta > 0$. The problem is to find

$$\mathbf{r} \quad s.t. \quad V_N(\mathbf{r}) - V_N \le c \log N$$

with c an universal constant. The corresponding problem related to $\beta = 0$ with $V_N(\mathbf{r}) = -\sum_{1\le i<j\le N} \log \|\mathbf{r}_i - \mathbf{r}_j\|$ is related to finding a good starting polynomial for a homotopy algorithm for realizing the fundamental theorem of algebra [2]. For $\beta = 1$, $V_N(\mathbf{r})$ is the Coulomb potential and finding the minimal energy configuration for N electrons on $\mathbb{S}^2$ is known as the Thomson problem [3]. But also other values of β are possible, $\beta = 3$ would model dipole interactions and $\beta = 12$ could be used to model the repulsive part of a Leonard-Jones potential.

*RB, AV and SP were supported by the DFG through Vo899/6-2 and Vo899/7-2.
MG and DP were supported by DFG through Po711/9-1 and Fi883/3-1.

†Institut für Wissenschaftliches Rechnen, TU Dresden, Zellescher Weg 12-14, 01062 Dresden, Germany (rainer.backofen@tu-dresden.de)

‡Fakultät für Mathematik, TU Chemnitz, Reichenheiner Str. 39, 09126 Chemnitz, Germany (m.graef@mathematik.tu-chemnitz.de).

§Fakultät für Mathematik, TU Chemnitz, Reichenheiner Str. 39, 09126 Chemnitz, Germany (potts@mathematik.tu-chemnitz.de).

¶Institut für Wissenschaftliches Rechnen, TU Dresden, Zellescher Weg 12-14, 01062 Dresden, Germany (simon.praetorius@tu-dresden.de)

‖Institut für Wissenschaftliches Rechnen, TU Dresden, Zellescher Weg 12-14, 01062 Dresden, Germany (axel.voigt@tu-dresden.de)

**Institut für Wissenschaftliches Rechnen, TU Dresden, Zellescher Weg 12-14, 01062 Dresden, Germany (thomas.witkowski@tu-dresden.de)

The criteria to be included in the "new set of Hilbert problems" are fulfilled: The problem is easy to formulate but not easy to solve and it is likely that its solution will have a large impact. Various numerical approaches have been applied to find an optimal distribution of N points on a sphere. However, the optimization problem becomes extremely difficult to solve for large N, as the number of local minima growth exponentially in N, see [4] for the Thomson problem. It remains to discuss the potential impact. Besides its importance in mathematics, i.e. for the mentioned application in algebra, ordering of interacting point on a sphere or more generally on curved surfaces, has also applications in different fields, e.g. water droplets in oil, which are coated with colloidal particles [5]. Such coated droplets are potential drug delivery vehicles [6, 7]. Similar configurations occur if a jammed layer of colloidal particles separates two immiscible fluids forming a so-called bijel [8], which has potential applications as an efficient micro-reacting media. A large number of ordered particles on curved surfaces is also required for fabrication of nanostructures on pliable substrates, e.g. to make foldable electronic devices [9]. Also viral capsides, where protein subunits play the role of the particles [10, 11, 12] are possible applications. The same is true for the head groups of lipid bilayers in biological membranes or self-assembled peptide nanostructures, see [13].

We will derive a continuum description to study the ordering of interacting particles on a sphere and describe three different numerical approaches which allow to obtain good approximations of V_N for large N. Our approach is based on energy minimization with the geometric frustration resulting from the curved surface incorporated. The paper is organized as follows: In Section 2 we derive a surface partial differential equation for a number density starting from N Brownian particles which interact via a pairwise repulsive potential $u(|\mathbf{r}_i - \mathbf{r}_j|) \approx 1/|\mathbf{r}_i - \mathbf{r}_j|^\beta$. In Section 3 we discuss different numerical approaches to solve the resulting nonlinear 6th order surface partial differential equation and compare them. In Section 4 we discuss results and in Section 5 we draw conclusions.

2. Model derivation. For the derivation we follow the approach of [14] in flat space: Assume N Brownian particles confined to a sphere which interact via a pairwise repulsive potential $u(|\mathbf{r}_i - \mathbf{r}_j|) \approx 1/|\mathbf{r}_i - \mathbf{r}_j|^\beta$. Neglecting inertial terms the motion of the particles can be described by N coupled surface Langevin equations $\dot{\mathbf{r}}_i = -\gamma^{-1}\nabla_{\Gamma,i}(\frac{1}{2}\sum_{i\neq j} u(|\mathbf{r}_i - \mathbf{r}_j|)) + \eta_i$ with γ a friction coefficient and η_i a Gaussian white noise random force term. Different ways have been shown in flat space how to derive from these equations a deterministic equation of motion for the time evolution of a particle density $\rho(\mathbf{r}) = \sum_i < \delta(\mathbf{r} - \mathbf{r}_i) >$, where $< . >$ denotes the ensemble average. This can either be done directly as shown in [15] or via a Smoluchovski equation as used in [16]. The continuity equation for ρ adapted to our situation on a curved surface than reads

$$\partial_t \rho = \gamma^{-1}\nabla_\Gamma \cdot (k_B T \nabla_\Gamma \rho + \int_\Gamma \rho^{(2)}(\mathbf{r}, \mathbf{r}')\nabla_\Gamma u(|\mathbf{r} - \mathbf{r}'|)\, \mathrm{d}\Gamma') \tag{2.1}$$

with $\rho^{(2)}(\mathbf{r}, \mathbf{r}') = \sum_{i,j} < \delta(\mathbf{r} - \mathbf{r}_i)\delta(\mathbf{r}' - \mathbf{r}_j) >$ the two-particle density and $k_B T$ the thermal energy. By approximating the two-particle density by its equilibrium counterpart and relating the last term in eq. (2.1) with the excess Helmholtz free energy functional $\mathcal{F}^\Gamma_{ex}[\rho]$, which is provided by classical density functional theory, we obtain the deterministic equation for the time-evolution of the one-particle density

$$\partial_t \rho = \gamma^{-1} k_B T \Delta_\Gamma \rho + \gamma^{-1}\nabla_\Gamma \cdot (\rho \nabla_\Gamma \frac{\delta \mathcal{F}^\Gamma_{ex}[\rho]}{\delta \rho})$$

which gives a dynamic density functional theory on a surface. As $\mathcal{F}^\Gamma_{ex}[\rho]$ is not known exactly for the potential u it has to be approximated. Following [17] and expanding $\mathcal{F}^\Gamma_{ex}[\rho]$ in terms of differences with a reference state $\bar{\rho}$ of an averaged density in the liquid phase, $\delta\rho = \rho - \bar{\rho}$ one obtains

$$\mathcal{F}^\Gamma_{ex}[\rho] \sim \mathcal{F}^\Gamma_{ex}[\bar{\rho}] - \frac{k_B T}{2} \int_\Gamma \int_\Gamma \delta\rho\delta\rho' c_0^{(2)}(\mathbf{r}-\mathbf{r}')\, d\Gamma d\Gamma'$$

with the direct correlation function $c_0^{(2)}(\mathbf{r}-\mathbf{r}')$ of the reference state $\bar{\rho}$. Following [18] by using this approximation and truncating a Taylor expansion of a Fourier transform of $c_0^{(2)}(\mathbf{r}-\mathbf{r}')$ on the sphere, we obtain

$$\partial_t \rho = \gamma^{-1} k_B T(\Delta_\Gamma \rho - \nabla_\Gamma \cdot (\rho \nabla_\Gamma((\hat{C}_0 - \hat{C}_2\Delta_\Gamma + \hat{C}_4\Delta_\Gamma^2)\rho))). \tag{2.2}$$

Instead of this physically derived model, we use the originally proposed phase field crystal model [19], which follows from eq. (2.2) by making further approximations, for details see [14], where both models are compared. Written as a system of three second order equations the model to be solved reads:

$$\partial_t \rho = \Delta_\Gamma \mu \tag{2.3}$$

$$\mu = 2\nu + \Delta_\Gamma \nu + f'(\rho) \tag{2.4}$$

$$\nu = \Delta_\Gamma \rho \tag{2.5}$$

with $f(\rho) = \frac{1}{2}(1-\epsilon)\rho^2 + \frac{1}{4}\rho^4$. This model was phenomenologically introduced in flat space, with Δ_Γ replaced by Δ as the H^{-1} gradient flow of the Swift-Hohenberg free energy

$$\mathcal{F}[\rho] = \int_\Omega -|\nabla\rho|^2 + \frac{1}{2}|\Delta\rho|^2 + f(\rho)\, \mathrm{d}\Omega \tag{2.6}$$

with $\Omega \subset \mathbb{R}^2$ in [19]. In the same way model (2.3) - (2.5) follow as the H^{-1} gradient flow of

$$\mathcal{F}^\Gamma[\rho] = \int_\Gamma -|\nabla_\Gamma\rho|^2 + \frac{1}{2}|\Delta_\Gamma\rho|^2 + f(\rho)\, \mathrm{d}\Gamma. \tag{2.7}$$

To relate the phase field crystal model to the original problem we have to parameterize it to approximate the direct correlation function of the reference state, which reflects the interatomic potential and might be computed using molecular dynamics on a small reference configuration. Various ways have been proposed how to do this approximation in two and three dimensions [19, 20, 14, 21]. The numerical results on a sphere however indicate, that the obtained minimal energy configurations are only sensitive to the defined lattice spacing (the position of the highest maxima in the direct correlation function) and insensitive to a large extend to other parameters. This might explain why triangular tessellations on spherical surfaces occur in very distinct occasions, for which the interactions involved may differ a lot.

In [22] the approach is validate for the Thomson problem $\beta = 1$ by computing minimal energy configurations for various numbers of N and comparing the resulting configurations and Coulomb energies with known results for $N \in [12, 2790]$. For $N \leq 112$ the computed configurations and energies coincide with the equilibrium values for the Thomson problem reported in [23]. The maximal deviation from the minimal energy for larger N is less than 0.1 %. In order to achieve this results, a small postprocessing step is needed. After identifying each maxima in the density field a gradient step is allowed to locally move the identified points [4]. The configuration thereby does not change but the Coulomb energy is slightly reduced.

3. Numerical approaches. Only recently various numerical methods have been proposed to solve a general class of partial differential equations on surfaces. They can be distinguished into direct methods, which require a surface mesh or points on a surface and indirect methods in which the surface is only implicitly described. Within the first approach parametric finite elements can be used to solve the surface partial differential equation, see e.g. [24, 25]. Other direct approaches consider finite volume discretizations, see e.g. [26]. Level set method have been used within the second approach, see e.g. [27]. Furthermore also phase-field models can be used to implicitly describe the surface, as used in [28, 29, 30, 31]. In order for the implicit approach to be efficient, adaptively refined meshes or narrow band approaches are required. For recent approaches in this direction see [32, 33, 34]. We will here concentrate on a phase-field approximation, a parametric finite element approach and a spectral method based on nonequispaced Fourier transforms on the sphere to solve eq. (2.3) - (2.5).

3.1. Phase field approximation. In [28] an approach is proposed how to solve partial differential equations on implicitly defined surfaces. Thereby the surface is represented by the 1/2-level set of a phase-field variable ϕ which is defined in a domain $\Omega \subset \mathbb{R}^3$ containing $\mathbb{S}^2$. However, the approach is not restricted to approximate partial differential equations on a sphere, but works for any surface Γ which can implicitly represented. Formally the approach results from an extension of the partial differential equation to Ω and multiplying all terms in their weak formulation by a surface delta function δ_Γ. For eq. (2.3)-(2.5) the resulting system reads

$$\begin{aligned}\delta_\Gamma \partial_t \rho &= \nabla \cdot (\delta_\Gamma \nabla \mu)\\ \delta_\Gamma \mu &= 2\nabla \cdot (\delta_\Gamma \nabla \rho) + \nabla \cdot (\delta_\Gamma \nabla \nu) + \delta_\Gamma f'(\rho)\\ \delta_\Gamma \nu &= \nabla \cdot (\delta_\Gamma \nabla \rho)\end{aligned}$$

with zero-flux boundary conditions on $\partial\Omega$ for ρ, μ and ν, and appropriate initial conditions for ρ. Within a next step we approximate

$$\delta_\Gamma \approx \frac{3\sqrt{2}}{\eta} B(\phi)$$

with $B(\phi) = \phi^2(1-\phi)^2$ and

$$\phi(\mathbf{x}, t) = \frac{1}{2}(1 + \tanh \frac{d(\mathbf{x})}{2\sqrt{2}\eta})$$

with η the diffuse interface thickness and $d(\mathbf{x})$ a signed distance function to the surface Γ. The system to solve now reads

$$B(\phi)\partial_t \rho = \nabla \cdot (B(\phi)\nabla \mu) \tag{3.1}$$

$$B(\phi)\mu = 2\nabla \cdot (B(\phi)\nabla \rho) + \nabla \cdot (B(\phi)\nabla \nu) + B(\phi) f'(\rho) \tag{3.2}$$

$$B(\phi)\nu = \nabla \cdot (B(\phi)\nabla \rho). \tag{3.3}$$

Matched asymptotic can be performed along the same lines as discussed in [28] for general parabolic systems of second order equations, to show the convergence to the original problem as $\eta \to 0$, see Appendix A.

In order to solve eq. (3.1) - (3.3) we use a semi-implicit time-discretization and Lagrange finite elements in space. The time interval is split by discrete time instants

$0 = t_0 < t_1 < \dots$ with time steps $\tau_m = t_m - t_{m-1}$. We linearize $f'(\rho^{(m+1)}) \approx f'(\rho^{(m)}) + f''(\rho^{(m)})(\rho^{(m+1)} - \rho^{(m)})$ and treat all other terms implicit. To discretize in space, let $\mathcal{T}_h$ be a conforming triangulation of Ω. We use the finite element space of globally continuous, piecewise linear elements $\mathbb{V}_h = \{v_h \in H^1 \,:\, v_h|_T \in \mathbb{P}^1 \; \forall T \in \mathcal{T}_h\}$. We thus obtain: Find $\rho_h^{(m+1)}$, $\mu_h^{(m+1)}$, $\nu_h^{(m+1)} \in \mathbb{V}_h$ such that

$$\begin{aligned}
\frac{1}{\tau_m}\int_\Omega B(\phi)\rho_h^{(m+1)}\xi \,\mathrm{d}x + \int_\Omega B(\phi)\nabla\mu_h^{(m+1)}\cdot\nabla\xi \,\mathrm{d}x &= \frac{1}{\tau_m}\int_\Omega B(\phi)\rho_h^{(m)}\xi \,\mathrm{d}x \\
\int_\Omega B(\phi)\mu_h^{(m+1)}\xi \,\mathrm{d}x + 2\int_\Omega B(\phi)\nabla\rho_h^{(m+1)}\cdot\nabla\xi \,\mathrm{d}x + \int_\Omega B(\phi)\nabla\nu_h^{(m+1)}\cdot\nabla\xi \,\mathrm{d}x & \\
-\int_\Omega f''(\rho_h^{(m)})\rho_h^{(m+1)}B(\phi)\xi \,\mathrm{d}x = \int_\Omega B(\phi)f'(\rho_h^{(m)})\xi \,\mathrm{d}x - \int_\Omega B(\phi)f''(\rho_h^{(m)})\rho_h^{(m)}\xi \,\mathrm{d}x & \\
\int_\Omega B(\phi)\nu_h^{(m+1)}\xi \,\mathrm{d}x + \int_\Omega B(\phi)\nabla\rho_h^{(m+1)}\cdot\nabla\xi \,\mathrm{d}x = 0. &
\end{aligned}$$

for all $\xi \in \mathbb{V}_h$. This leads to a linear system of equations for $R^{(m+1)}$, $M^{(m+1)}$ and $N^{(m+1)}$) with $\rho_h^{(m+1)} = \sum_i R_i^{(m+1)}\xi_i$, $\mu_h^{(m+1)} = \sum_i M_i^{(m+1)}\xi_i$ and $\nu_h^{(m+1)} = \sum_i N_i^{(m+1)}\xi_i$

$$\begin{aligned}
\frac{1}{\tau_m}\mathbf{M}R^{(m+1)} + \mathbf{A}M^{(m+1)} &= \frac{1}{\tau_m}\mathbf{M}R^{(m)} \\
\mathbf{M}M^{(m+1)} + 2\mathbf{A}R^{(m+1)} + \mathbf{A}N^{(m+1)} - \mathbf{F}^i R^{(m+1)} &= \mathbf{F}^e \\
\mathbf{M}N^{(m+1)} + \mathbf{A}R^{(m+1)} &= 0
\end{aligned}$$

with

$$\begin{aligned}
\mathbf{M} = (M_{ij}) \quad & M_{ij} = (B(\phi)\xi_i, \xi_j)_\Omega \\
\mathbf{A} = (A_{ij}) \quad & A_{ij} = (B(\phi)\nabla\xi_i, \nabla\xi_j)_\Omega \\
\mathbf{F}^i = (F_{ij})^i \quad & F_{ij}^i = (B(\phi)f''(\rho_h^{(m)})\xi_i, \xi_j)_\Omega \\
\mathbf{F}^e = (F_i)^e \quad & F_i^e = (B(\phi)(f'(\rho_h^{(m)}) - f''(\rho_h^{(m)}))\rho_h^{(m)}, \xi_i)_\Omega
\end{aligned}$$

where $(\cdot,\cdot)_\Omega$ denotes the L^2-scalar product in Ω. The resulting system is iteratively solved using BiCGStab(ell). In order for the approach to be efficient we use an adaptively refined mesh along the 1/2-level set of the phase-field function ϕ. Within the diffuse interface we require $h < \eta$ with approximately 10 grid points across the interface. We further require $\eta < a$, with a the equilibrium lattice constant in the phase field crystal model. Fig. 3.1 shows a typical mesh together with the phase field variable ϕ describing the surface and the solution for ρ on the 1/2-level set of ϕ in Ω.

3.2. Parametric finite elements. A more direct approach solves eq. (2.3)-(2.5) on a surface mesh. In a parametric finite element approach instead of performing the integration on the surface elements T of a surface triangulation $\mathcal{T}$ of $\mathbb{S}^2$, a parameterization $F_T : \hat{T} \to T$ is used, with $\hat{T} = \text{conv hull}\,\{0, \vec{e}_1, \vec{e}_2\}$ the *standard element* in $\mathbb{R}^2$. Furthermore we can define the basis functions on a *reference element* $\overline{T} = \{(\lambda_0, \dots, \lambda_2) \in I\!R^3; \lambda_k \geq 0, \sum_{k=0}^2 \lambda_k = 1\}$ using barycentric coordinates. These allow to transform all integrations onto the *standard element* and have the definition of basis functions on the *reference element* at hand. Both are defined in $\mathbb{R}^2$ and $\mathbb{R}^3$. The parameterization F_T is given by the coordinates of the surface mesh elements and provides the only difference between solving equations on surfaces and on planar

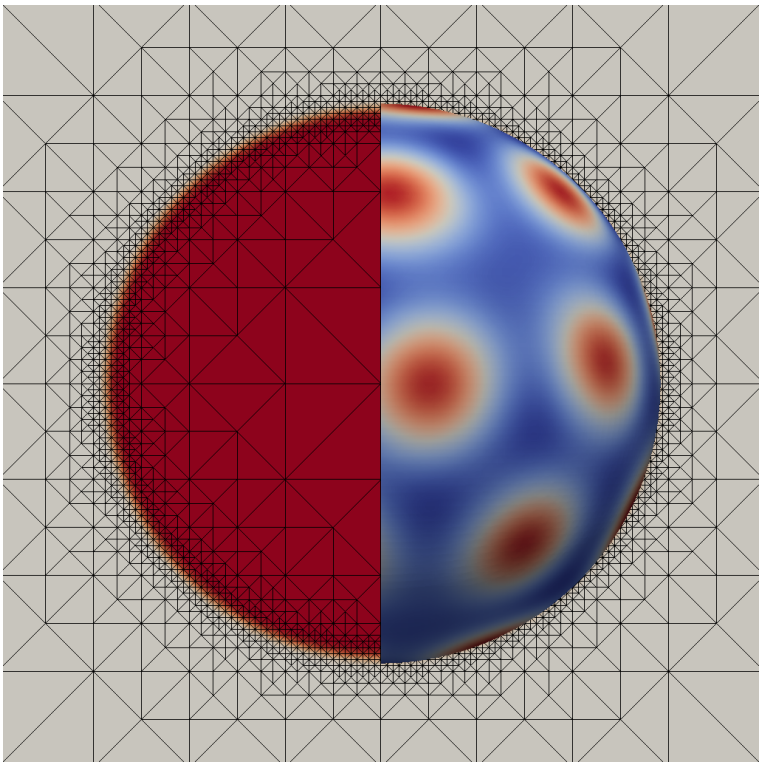

Fig. 3.1. *Adaptively refined mesh along* 1/2*-level set of* ϕ *representing* $\mathbb{S}^2$*, solution for* ρ *in on* 1/2*-level set and phase field variable.*

domains. For a surface we have to allow $F_T : \mathbb{R}^2 \to \mathbb{R}^3$, whereas for a planar domain $F_T : \mathbb{R}^2 \to \mathbb{R}^2$. With this tiny modification any code to solve partial differential equations on Cartesian grids can be used to solve the same problem on a surface, providing a surface triangulation is given. Again the approach is therefor not restricted to $\mathbb{S}^2$ but works for any triangulated surface. Within an efficient implementation this does not even require to recompile a running 2D code, but only a change in a parameter file, as e.g. done in AMDiS [25] . With this approach all available tools to solve partial differential equations on planar domains, such as adaptive refinement, multigrid algorithms or parallelization approaches, can be used also to solve partial differential equations on surfaces, see e.g. [25, 35, 36].

To solve eq. (2.3)-(2.5) we use the discretization scheme introduced in [37], with the integration defined on the discrete surface mesh. Similar to the above scheme we use a semi-implicit time-discretization and Lagrange finite elements in space. The time interval is split by discrete time instants $0 = t_0 < t_1 < \dots$ with time steps $\tau_m = t_m - t_{m-1}$. We linearize $f'(\rho^{(m+1)}) \approx f'(\rho^{(m)}) + f''(\rho^{(m)})(\rho^{(m+1)} - \rho^{(m)})$ and treat all other terms implicit. To discretize in space, let Γ_h be a conforming triangulation of Γ. We use the finite element space of globally continuous, piecewise quartic elements $\mathbb{V}_h = \{v_h \in H^1 \ : \ v_h|_T \in \mathbb{P}^4 \ \forall T \in \Gamma_h\}$. We thus obtain: Find

$\rho_h^{(m+1)}$, $\mu_h^{(m+1)}$, $\nu_h^{(m+1)} \in \mathbb{V}_h$ such that

$$\begin{aligned}
&\frac{1}{\tau_m}\int_{\Gamma_h} \rho_h^{(m+1)}\xi \,\mathrm{d}\Gamma_h + \int_{\Gamma_h} \nabla_{\Gamma_h}\mu_h^{(m+1)} \cdot \nabla_{\Gamma_h}\xi \,\mathrm{d}\Gamma_h = \frac{1}{\tau_m}\int_{\Gamma_h} \rho_h^{(m)}\xi \,\mathrm{d}\Gamma_h \\
&\int_{\Gamma_h} \mu_h^{(m+1)}\xi \,\mathrm{d}\Gamma_h + 2\int_{\Gamma_h} \nabla_{\Gamma_h}\rho_h^{(m+1)} \cdot \nabla_{\Gamma_h}\xi \,\mathrm{d}\Gamma_h + \int_{\Gamma_h} \nabla_{\Gamma_h}\nu_h^{(m+1)} \cdot \nabla_{\Gamma_h}\xi \,\mathrm{d}\Gamma_h \\
&-\int_{\Gamma_h} f''(\rho_h^{(m)})\rho_h^{(m+1)}\xi \,\mathrm{d}\Gamma_h = \int_{\Gamma_h} f'(\rho_h^{(m)})\xi \,\mathrm{d}\Gamma_h - \int_{\Gamma_h} f''(\rho_h^{(m)})\rho_h^{(m)}\xi \,\mathrm{d}\Gamma_h \\
&\int_{\Gamma_h} \nu_h^{(m+1)}\xi \,\mathrm{d}\Gamma_h + \int_{\Gamma_h} \nabla_{\Gamma_h}\rho_h^{(m+1)} \cdot \nabla_{\Gamma_h}\xi \,\mathrm{d}\Gamma_h = 0.
\end{aligned}$$

for all $\xi \in \mathbb{V}_h$. This leads to a linear system of equations for $R^{(m+1)}$, $M^{(m+1)}$ and $N^{(m+1)}$ with $\rho_h^{(m+1)} = \sum_i R_i^{(m+1)}\xi_i$, $\mu_h^{(m+1)} = \sum_i M_i^{(m+1)}\xi_i$ and $\nu_h^{(m+1)} = \sum_i N_i^{(m+1)}\xi_i$

$$\begin{aligned}
\frac{1}{\tau_m}\mathbf{M}R^{(m+1)} + \mathbf{A}M^{(m+1)} &= \frac{1}{\tau_m}\mathbf{M}R^{(m)} \\
\mathbf{M}M^{(m+1)} + 2\mathbf{A}R^{(m+1)} + \mathbf{A}N^{(m+1)} - \mathbf{F}^i R^{(m+1)} &= \mathbf{F}^e \\
\mathbf{M}N^{(m+1)} + \mathbf{A}R^{(m+1)} &= 0
\end{aligned}$$

with

$$\begin{aligned}
\mathbf{M} = (M_{ij}) \quad & M_{ij} = (\xi_i, \xi_j)_{\Gamma_h} \\
\mathbf{A} = (A_{ij}) \quad & A_{ij} = (\nabla_{\Gamma_h}\xi_i, \nabla_{\Gamma_h}\xi_j)_{\Gamma_h} \\
\mathbf{F}^i = (F_{ij})^i \quad & F_{ij}^i = (f''(\rho_h^{(m)})\xi_i, \xi_j)_{\Gamma_h} \\
\mathbf{F}^e = (F_i)^e \quad & F_i^e = ((f'(\rho_h^{(m)}) - f''(\rho_h^{(m)}))\rho_h^{(m)}, \xi)_{\Gamma_h}
\end{aligned}$$

where $(\cdot,\cdot)_{\Gamma_h}$ denotes the L^2-scalar product on Γ_h. The resulting system is solved using the direct solver paradiso. We use a surface mesh which results from adaptive refinement by bisection and projection of the inserted nodes on $\mathbb{S}^2$, starting from a cube with 12 triangular elements, see Fig. 3.2 for a sequence of refined meshes.

3.3. Spectral method. In many applications, where nonlinear partial differential equations have to be solved on flat spaces, so-called Fourier spectral techniques have proven to be very efficient and accurate, cf. [38, 39]. These methods benefit from exponential convergence rates for smooth solutions and from fast Fourier transforms like the FFT. The proposed approach is based on the expansion of a function $f \in \mathrm{L}^2(\mathbb{S}^2)$ in spherical harmonics Y_l^m, $l \in \mathbb{N}_0$, $m = -l, \dots, l$, which are eigenfunctions of the spherical Laplace operator $\Delta_{\mathbb{S}^2}$, cf. [40].

Let the sphere $\mathbb{S}^2$ of radius $r > 0$ be parameterized by spherical coordinates $(\vartheta, \varphi) \in [0, \pi] \times [0, 2\pi)$ with $\mathbf{x}(\vartheta, \varphi) := (r\sin\vartheta\cos\varphi, r\sin\vartheta\sin\varphi, r\cos\vartheta)$. Then the spherical harmonics of degree $l \in \mathbb{N}_0$ and order $m = -l, \dots, l$ can be represented by

$$Y_l^m(\mathbf{x}) = Y_l^m(\vartheta, \varphi) := \sqrt{\frac{2l+1}{4\pi r^2}} P_l^{|m|}(\cos\vartheta)\mathrm{e}^{\mathrm{i}m\varphi}.$$

For the readers convenience, the associated Legendre functions $P_l^m : [-1, 1] \to \mathbb{R}$ and

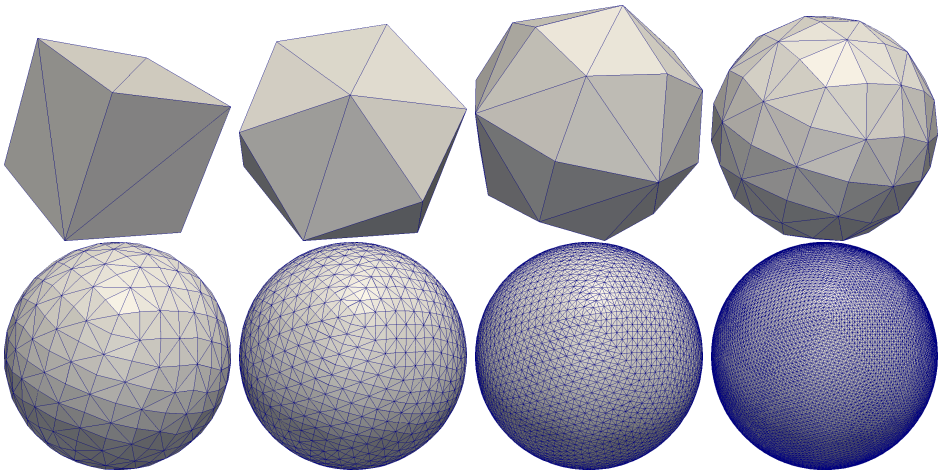

Fig. 3.2. *Sequence of surface meshes approximating* $\mathbb{S}^2$.

the Legendre polynomials $P_l : [-1,1] \to \mathbb{R}$ are given by

$$P_l^m(x) = \left(\frac{(l-m)!}{(l+m)!}\right)^{1/2} \left(1-x^2\right)^{m/2} \frac{\mathrm{d}^m}{\mathrm{d}x^m} P_l(x), \qquad l \in \mathbb{N}_0,\ m \le l,$$

$$P_l(x) := \frac{1}{2^l l!} \frac{\mathrm{d}^l}{\mathrm{d}x^l} \left(x^2-1\right)^l, \qquad l \in \mathbb{N}_0.$$

The spherical harmonics Y_l^m form an orthonormal basis of $\mathrm{L}^2(\mathbb{S}^2)$. Hence, every function $f \in \mathrm{L}^2(\mathbb{S}^2)$ obeys the series expansion

$$f = \sum_{l \in \mathbb{N}_0} \sum_{m=-l}^{l} \hat{f}_l^m Y_l^m$$

with spherical Fourier coefficients

$$\hat{f}_l^m := \int_{\mathbb{S}^2} f(\mathbf{x}) Y_l^m(\mathbf{x}) \mathrm{d}\mathbf{x}, \quad l \in \mathbb{N}_0,\ m = -l, \dots, l.$$

Furthermore we denote by $\Pi_n(\mathbb{S}^2) := \{f = \sum_{l=0}^n \sum_{m=-l}^l \hat{f}_l^m Y_l^m\}$ the space of all spherical polynomials with degree at most n and we remark that its dimension is $d_n := (n+1)^2$.

The spectral methods are based on the ansatz to approximate the solutions of partial differential equation by spherical polynomials. We approximate the solution ρ of eq. (2.3) - (2.5) by the spherical polynomial

$$\rho_n(\mathbf{x},t) := \sum_{l=0}^{n} \sum_{m=-l}^{l} \hat{\rho}_l^m(t) Y_l^m(\mathbf{x}).$$

In order to determine the spherical Fourier coefficients $\hat{\rho}_l^m = \hat{\rho}_l^m(t)$ we use Galerkins method, cf. [39, Ch. 3], which requires that for every $t > 0$ the residual

$$R_n(\mathbf{x},t) := \partial_t \rho_n(\mathbf{x},t) - \Delta_{\mathbb{S}^2} \left[\left((\Delta_{\mathbb{S}^2} + 1)^2 - \varepsilon \right) \rho_n(\mathbf{x},t) + \rho_n(\mathbf{x},t)^3 \right] \tag{3.4}$$

is orthogonal to $\Pi_n(S^2)$. Since the spherical harmonics are eigenfunctions of the spherical Laplacian, i.e.,

$$\Delta_{\mathbb{S}^2} Y_l^m = -\frac{l(l+1)}{r^2} Y_l^m, \quad l \in \mathbb{N}_0,\ l = -m, \dots, m,$$

we obtain to equation (3.4) the equivalent system of ordinary differential equations in the Fourier domain

$$\frac{\mathrm{d}\hat{\rho}_l^m}{\mathrm{d}t} = -\frac{l(l+1)}{r^2}\left[\left(\left(1 - \frac{l(l+1)}{r^2}\right)^2 - \varepsilon\right)\hat{\rho}_l^m + (\widehat{\rho_n^3})_l^m\right], \tag{3.5}$$

with $l = 0, \dots, n$, $m = -l, \dots, l$. In order to solve the nonlinear system (3.5) numerically it is common praxis to use semi-implicit schemes, where one treats the linear terms implicitly and the nonlinear term explicitly, cf. [41]. Here we use a second-order backward difference for the linear term and a second-order Adams-Bashforth scheme for the nonlinear term. For simplicity we omit the indices l and m of the spherical Fourier coefficients $\hat{\rho}_l^m$, $(\widehat{\rho_n^3})_l^m$ and indicate the t-th iterated of the scheme by $\hat{\rho}_t$ and $(\widehat{\rho_n^3})_t$ respectively. With the time step τ the scheme reads as

$$\begin{aligned}\frac{3\hat{\rho}_{t+1} - 4\hat{\rho}_t + \hat{\rho}_{t-1}}{2\tau} &= \\ -\frac{l(l+1)}{r^2}&\left[\left(\left(1 - \frac{l(l+1)}{r^2}\right)^2 - \varepsilon\right)\hat{\rho}_{t+1} + \left(2(\widehat{\rho_n^3})_t - (\widehat{\rho_n^3})_{t-1}\right)\right],\end{aligned} \tag{3.6}$$

where the first step is computed by the corresponding first-order scheme

$$\frac{\hat{\rho}_1 - \hat{\rho}_0}{\tau} = -\frac{l(l+1)}{r^2}\left[\left(\left(1 - \frac{l(l+1)}{r^2}\right)^2 - \varepsilon\right)\hat{\rho}_1 + (\widehat{\rho_n^3})_0\right] \tag{3.7}$$

with initial spherical Fourier coefficients $\hat{\rho}_0$.

For the computation of the above spherical Fourier coefficients $\hat{\rho}_t$ we shall use fast Fourier transforms on the sphere $\mathbb{S}^2$. For a more convenient notation we introduce for arbitrary scattered sampling nodes $\mathcal{X} := \{\mathbf{x}_1, \dots, \mathbf{x}_M\} \subset \mathbb{S}^2$ the nonequispaced spherical Fourier matrix

$$\mathbf{Y} := (Y_l^m(\mathbf{x}_i))_{i=0;\ l=0,\ m=-l}^{M,\ n,\ l} \in \mathbb{C}^{M \times d_n}.$$

By means of the matrix-vector notation the point evaluation of the spherical polynomial ρ_n on the nodes $\mathcal{X}$ can be written as

$$\boldsymbol{\rho}_n = \mathbf{Y}\widehat{\boldsymbol{\rho}_n},$$

where $\boldsymbol{\rho}_n := (\rho_n(x_i))_{i=1}^M \in \mathbb{C}^M$ are the sampling values and $\widehat{\boldsymbol{\rho}_n} := (\widehat{\boldsymbol{\rho}}_l^m)_{l=0,\ m=-l}^{n,\ l} \in \mathbb{C}^{d_n}$ is the corresponding Fourier coefficient vector. Recently, fast algorithms for the matrix times vector multiplication with the nonequispaced spherical Fourier matrix $\mathbf{Y}$ and its adjoint $\mathbf{Y}^*$ have been proposed in [42]. Both algorithms have an arithmetic complexity of $\mathcal{O}(n^2 \log^2 n + M)$ and are implemented in the NFFT library [43].

As already seen, the multiplication with the spherical Fourier matrix $\mathbf{Y}$ is nothing else than the evaluation of a spherical polynomial. For the analysis step, that is the computation of Fourier coefficients $\widehat{\boldsymbol{\rho}_n}$, we can make use of the fast adjoint spherical

Fourier transform in conjunction with suitable quadrature rules, cf. [44]. More precisely, a quadrature rule on the sphere $\mathbb{S}^2$ is a set of pairs $(\mathbf{x}_i, w_i)$, $i = 1, \dots, M$, with sample nodes $\mathbf{x}_i \in \mathbb{S}^2$ and quadrature weights $w_i \in \mathbb{C}$. We say such a rule has degree of exactness n if

$$\sum_{i=0}^{M} w_i p(\mathbf{x}_i) = \int_{\mathbb{S}^2} p(\mathbf{x}) \mathrm{d}\mathbf{x}$$

is valid for all spherical polynomials $p \in \Pi_n(\mathbb{S}^2)$. Hence, given a quadrature with degree of exactness $2n$ we can reconstruct the Fourier coefficients $\widehat{\boldsymbol{\rho}_n}$ of the spherical polynomial ρ_n from its sample values. In matrix-vector notation this is done by multiplication with the adjoint $\mathbf{Y}^*$ and the weight matrix $\mathbf{W} = \operatorname{diag}(w_i)_{i=1}^M$

$$\widehat{\boldsymbol{\rho}_n} = \mathbf{Y}^* \mathbf{W} \boldsymbol{\rho}_n. \tag{3.8}$$

Recently, efficient algorithms for the computation of the weights w_i for scattered sampling nodes $\mathcal{X}$ have been proposed in [45]. Since we are not able to compute the Fourier coefficients of the nonlinear term ρ_n^3 explicitly, we are forced to switch in every time step (3.6) between the spatial and Fourier domain. There we evaluate first from the Fourier coefficients $\widehat{\boldsymbol{\rho}_n}$ the sample values $\boldsymbol{\rho}_n$. From these we simply obtain the cubed values and compute by means of the adjoint spherical Fourier transform in conjunction with a quadrature rule the spherical Fourier coefficients $(\widehat{\rho_n^3})_l^m$. We remark that if the initial value $\rho_0 \in \Pi_n(\mathbb{S}^2)$ and the used quadrature rules have degree of exactness $4n$ we compute in every step the exact projected spherical Fourier coefficients of the time-discretized Galerkin-method.

The above discussed semi-implicit scheme (3.6), (3.7) is implemented in Matlab R2009b, where the mex-interface to the NFFT library [43] is used. For the NFSFT (nonequispaced fast spherical Fourier transforms) we set the flags PRE_PSI and PRE_PHI_HUT, the threshold parameter $\kappa = 1000$ and the cutoff parameter $m = 9$. For the sampling nodes we used a slightly modified Reuter grid, cf. [46, Ex. 7.1.9].

$$X := \{\mathbf{x}(0,0), \mathbf{x}(\pi,0)\} \cup \bigcup_{j=1}^{S-1} \left\{ \mathbf{x}\left(\frac{j\pi}{S}, \left(k - \frac{1}{2}\mathrm{mod}(j,2)\right)\left(\frac{2\pi}{S_j}\right)\right) : k = 1, \dots, S_j \right\}$$

$$\text{with} \qquad S_j := 5 \left\lfloor \sqrt{3}\pi / \arccos\left(\left(\cos\frac{\pi}{S} - \cos^2\frac{j\pi}{S} \right) / \sin^2\frac{j\pi}{S} \right) / 5 \right\rfloor .$$

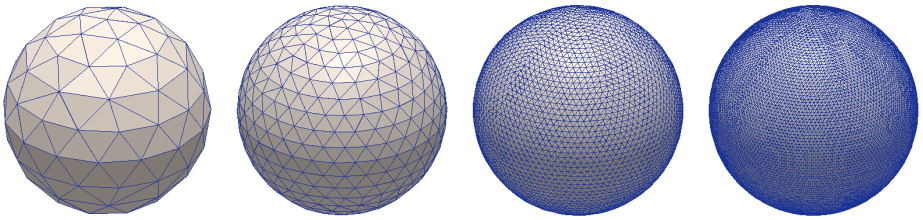

Fig. 3.3. *Sequences of the slightly modified Reuter grids.*

We found that for this grid it is sufficient to use $M \approx 100N$ sampling nodes, where N is the number of expected maxima of the density function ρ. Furthermore, the

Figure 4.5 in Section 4 shows that for a suitable solution the most important spherical Fourier coefficients, besides the first $\hat{\rho}_0^0$, are located in a band around the degree $n \approx r$. Furthermore we computed the quadrature weights for this grid accordingly due to [45]. Hence the evaluation of (3.8) reproduces the spherical Fourier coefficients of a polynomial with requested degree n.

4. Results. A classic theorem of Euler shows for a triangulation of the surface in which nearest neighbors are connected, that $\sum_i (6-i)v_i = 6\chi$, with v_i the number of vertices with i nearest neighbors and χ the Euler characteristic of the surface. Thus for surfaces with the topology of a sphere ($\chi = 2$), besides the expected triangular lattice with six-fold coordination, which would give the optimal ordering in $\mathbb{R}^2$, there must be at least 12 five-fold disclinations present. With each disclination an extra energy is associated (relative to a perfect triangular lattice in flat space) which grows proportional to r^2, with r the radius of the sphere. For a fixed lattice constant a we have $N \sim (r/a)^2$. Thus for large N, or respectively large r, mechanisms are expected which reduce this extra energy by changing the ground state configuration, which can be done by introducing additional defects and forming so-called grain boundary scars, which are chains of five-fold and seven-fold disclinations. Experimental results for such configurations have been observed in [5]. For a detailed discussion we refer to [13].

We will use our numerical approaches to first show minimal energy configurations for small N, for which 12 isolated five-fold disclinations provide the global minimum. Next we consider larger N and compare the different numerical schemes. We demonstrate energy reduction in time and the obtained minimal energy configuration with additional defect structures. Last we show the potential for each of the numerical methods by going to even larger N, by generalizing the surface to be considered and discussing extensions to couple the ordering with the evolution of the surface.

4.1. Isolated disclinations. For $2 \leq N \leq 100$ there is agreement of all numerical and theoretical methods, suggesting that the global minimum configuration V_N has been found. The most prominent configuration is certainly known for $N = 32$ which result in 12 isolated 5-fold disclinations. A Voronoi pattern for this configuration can be found in a typical soccer ball. The same configuration is obtained with all three numerical approaches, see Fig. 4.1. The memory requirements and computational time needed to obtain the result however differs, see Tab. 4.1. The degrees of freedom (DOFs) for the NFFT approach are given by the dimension d_n of the underlying polynomial space Π_n.

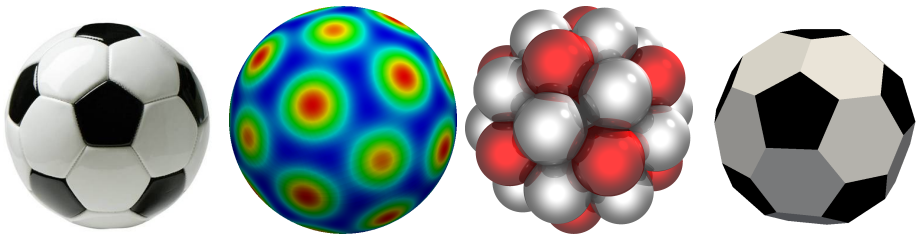

FIG. 4.1. *Typical soccer ball and minimal energy configuration for $N = 32$. (middle) density field, (right) visualization of extracted maxima in density field, colour coding according to number of neighbors*

	CPU-time	Memory	DOFs
NFFT	20 s	300 MB	289
parametric FEM	1020 s	180 MB	18.438
phase field approximation	140 h	1.4 GB	217.301

Table 4.1

Comparison of the three numerical approaches for $N = 32$. The parameters used are $\epsilon = 0.4$, $\bar{\rho} = -0.3$. We start with a randomly perturbed initial configuration $\rho_0 = \bar{\rho} \pm 0.05$ and measure the CPU-time required to reach $t = t_{end}$ for which the equilibrium configuration is achieved. The time steps used for each method differ. In case of the NFFT the reported memory requirement is the allocated memory by Matlab.

4.2. Grain boundary scars. Grain boundary scars (chains of 5-fold and 7-fold disclinations) are expected for $N > 360$. Realizations where the formation of grain boundary scars has been observed are for example water droplets in oil, which are coated with colloidal particles [5]. In contrast to grain boundaries in flat space grain boundary scars on curved surfaces belong to the equilibrium state. Furthermore they freely terminate which is not the case for grain boundaries in $\mathbb{R}^2$ or $\mathbb{R}^3$.

In order to demonstrate the comparability of the different numerical approaches we consider a configuration with $N = 492$. Instead of a randomly perturbed initial state we use a defined state and monitor not only the equilibrium configuration but also the evolution of the different approaches. The initial state is given on a sphere with radius $r = 42$ by

$$\rho_0(\mathbf{r}) := -0.26 \left(1 - 2 \sum_{i=1}^{4} \mathrm{e}^{-500 \arccos(\mathbf{r}\cdot\mathbf{r}_i/42)^2} \right)$$

with $\mathbf{r}_i$ the vertices of the tetrahedron. Due to the high computational cost of the phase-field approach we only consider the parametric FEM and the NFFT approach. Fig. 4.2 shows the obtained equilibrium configuration, which coincide for both approaches. Fig. 4.3 shows a comparison of the two approaches.

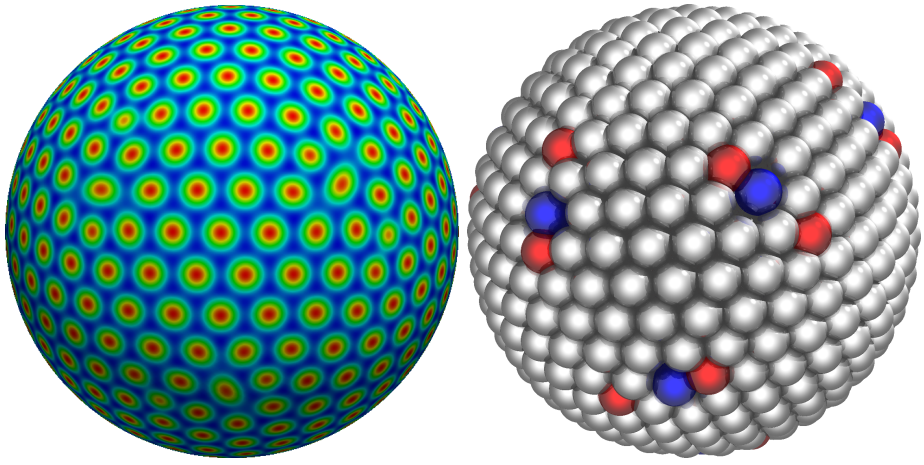

Fig. 4.2. *Density field and particle visualization of obtained minimal energy configuration for $N = 492$, colour coding according to number of neighbors.*

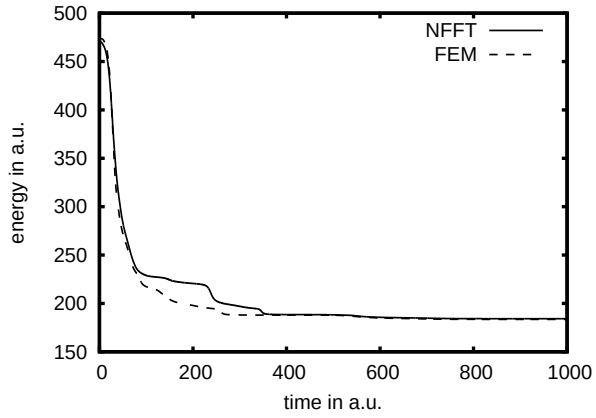

FIG. 4.3. *Decay in energy over time for minimization problem. The difference in the dynamics results from different time step strategies used in the FEM and the NFFT algorithms.*

The corresponding Coulomb energy of the computed configuration is $V_{492}(\mathbf{r}) = 115006.5738019$, which is slightly above the communicated minimal energy $V_{492} = 115005.0932623$, which corresponds to a configuration in which the 12 five-fold disclinations are not isolated but form 12 chains with the pairs of five-fold and seven-fold disclinations [4].

4.3. Other examples and comparison of the numerical approaches. As a last example on a sphere we consider a configuration with $N \approx 100000$ to show the potential of the approach to find good estimates for V_N if N is large. Fig. 4.4 shows the obtained minimal energy configuration using the NFFT approach, which turned out to be the most efficient method on a sphere. There we used an icosahedral symmetric initial state with density $\bar{\rho} = -0.3$ on a sphere with radius $r = 600$. We have chosen the parameter $\epsilon = 0.25$ for a slow crystal growth up to the time $t = 2500$ and increased it to $\epsilon = 0.4$ for another time-length of $t = 1500$ in order to freeze the configuration. The simulation took about 1.5 days on a single processor with 12GB RAM. After locating the $N = 99602$ maxima we computed the energy $V_N(\mathbf{r}) \approx 4.942914 \cdot 10^9$ which is less than 0.0004% above the lower bound $\frac{1}{2}N^2 - 0.553051N^{3/2} \approx 4.942895 \cdot 10^9$ from [47]. Furthermore under the given initial distribution one observes a similar star structure of the defects of the minimal configuration as predicted in [48]. In this example we obtain 732 defects which come in pairs of 5-fold and 7-fold defects located along lines connecting 12 5-fold defects, which are located at the vertices of an icosahedron.

For the above example we used for the approximation a polynomial degree $n = 900$ and a modified Reuter grid with parameter $S = 3000$ which has approximately 10 million sampling nodes. For this grid we computed the quadrature weights for a degree of exactness $n = 1024$. Figure 4.5 shows the absolute values of the spherical Fourier coefficients $\hat{\boldsymbol{\rho}}$ of the density ρ at time $t = 3000$. There is seen that the equilibrium state admits a relatively sparse representation in spherical harmonics, i.e., the most Fourier coefficients are nearby zero.

In contrast to the NFFT approach, which turned out to be the most efficient on a sphere the parametric FEM approach is not restricted to $\mathbb{S}^2$. It can be used on any parametric surface. To demonstrate this we use the approach on the Stanford

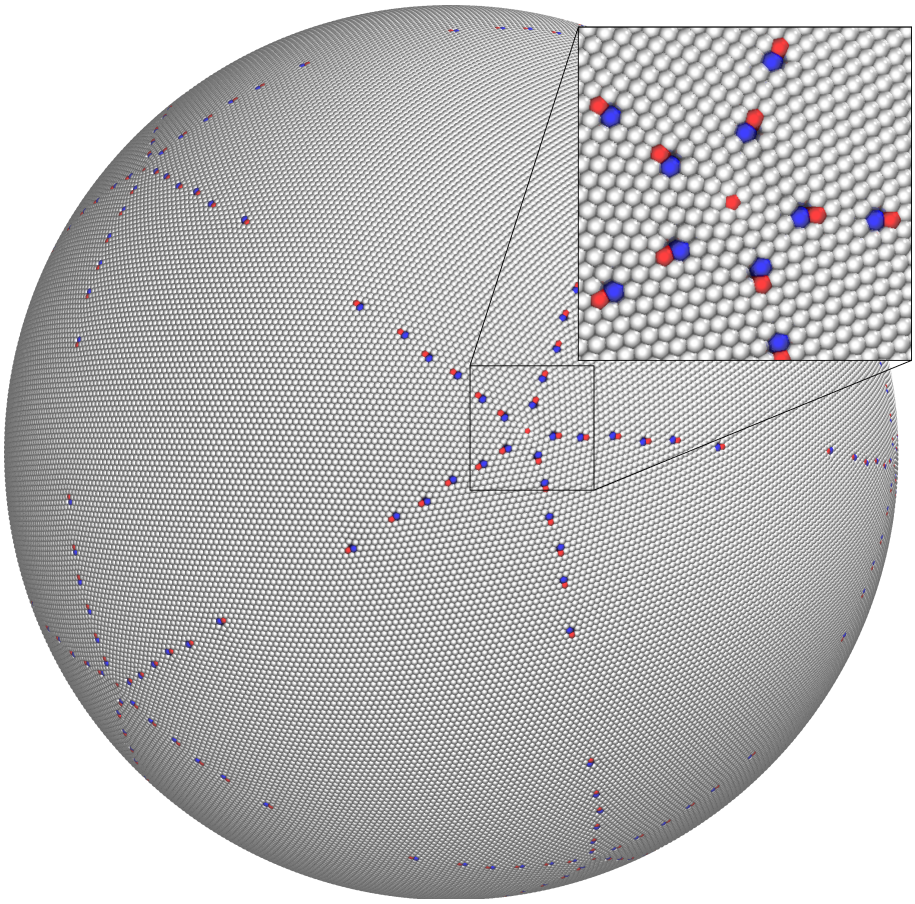

Fig. 4.4. *Particle visualization of obtained minimal energy configuration for $N = 99602$, colour coding according to number of neighbors.*

bunny. Fig. 4.6 shows the obtained minimal energy configuration using parametric FEM starting from a randomly perturbed initial configuration.

The only requirement for the surface is an appropriate surface mesh. The computational cost does not depend on the morphology of the surface, but only the number of grid points. The approach can be parallelized, using the same techniques as used to parallelize standard FEM. In [36] various of these techniques are discussed and applied to solve surface partial differential equations. The ability of the approach to work on arbitrary surfaces will also allow to consider ordering on evolving surfaces. Appropriate continuum models for such evolutions, which account for bending and surface tension are discussed in the mathematical review article [49, 50]. Different concepts have been developed to solve differential equations on evolving surfaces [24] in the context of parametric FEM. This concept however, can induce severe mesh distortions as a result of the evolution and requires additional treatment of mesh points to maintain appropriate mesh properties.

Within the considered phase-field description such problems do not occur. An extension of the method in [28] to evolving surfaces is discussed in [29, 30, 31]. It is the most flexible and most straight forward to implement approach, as it does not

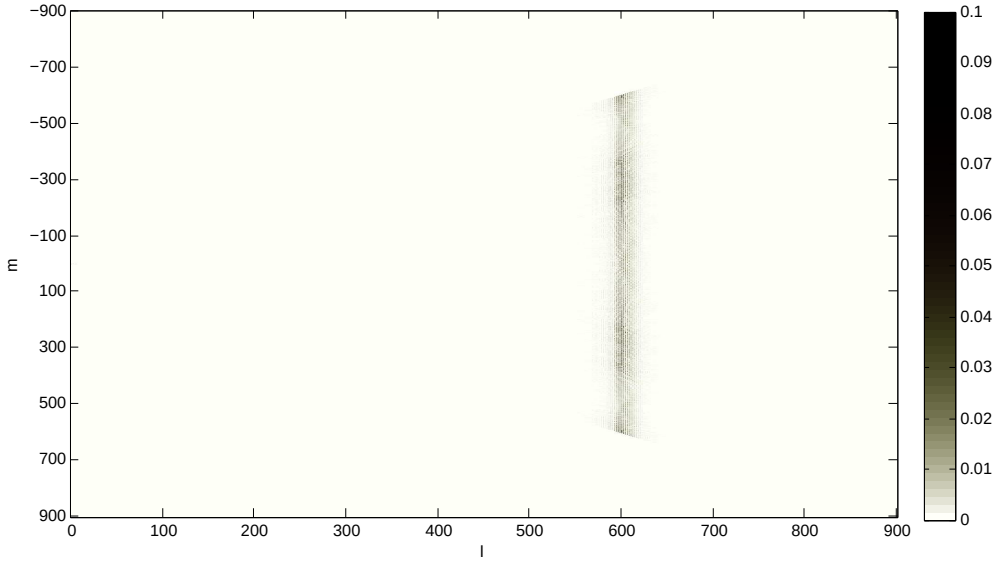

FIG. 4.5. *Visualization of the Fourier coefficients of the equilibrium state. One observes that the most relevant Fourier coefficients are located in a band about* $l = 600$.

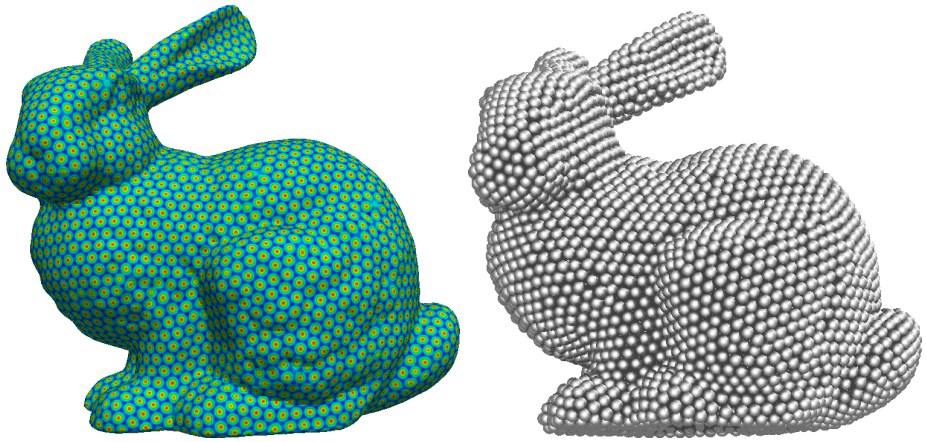

FIG. 4.6. *Density field and particle visualization of obtained minimal energy configuration for* $N = 3303$ *on the Stanford bunny.*

require any special treatment, but it is also to most expensive method as it operates in one dimension higher. The coupling of the surface evolution with the evolution of the number density on it, however remains open for all methods and requires further developments.

5. Conclusion. Using the approach introduced in [22] to find optimal configurations of interacting particles on a sphere, we consider different numerical approaches to solve the 6th order surface partial differential equation. Besides parametric finite elements and phase-field descriptions which are adapted to solve the specific equation, a new computational approach is introduced. The introduced spectral method is based on the ansatz to approximate the solution of the surface partial differential

equation by spherical polynomials. For the computation of the spherical Fourier coefficients a fast Fourier transforms on the sphere with nonequispaced nodes is used. By making the Fourier spectral techniques available on a sphere a general approach is introduced which benefits from exponential convergence rates and turns out to be computationally much more efficient than the previously discussed methods to solve surface partial differential equations. This is demonstrated here for a specific application, but we believe that the benefits of the approach will carry over to all problems which are efficiently solved using Fourier spectral methods in $\mathbb{R}^2$ or $\mathbb{R}^3$ if considered on a sphere. The other discussed numerical approach, turn out to be less efficient but much more flexible concerning the surface to be considered. The parametric finite element approach only requires an appropriate surface mesh and shows a computational cost which is independent on the complexity of the surface, only depending on the number of nodes. Within the phase-field description the surface partial differential equation is reformulated into a partial differential equation in $\mathbb{R}^3$ and can be solved with any standard approach. For computational efficiency, however, adaptivity is recommended, allowing for a fine resolution along the approximated surface and a coarse triangulation otherwise.

Concerning the specific application we have shown how to relate the interatomic potential describing the particle interactions on the sphere with the parameters in the surface partial differential equation. The derivation of the model extends an approach in flat space and uses a dynamic density functional theory on surfaces. Examples of computed minimal energy configurations show the applicability of the approach to solve the originally formulated optimization problem. The question of finding the global minimum with the approach remains open. As the approach is constructed as an energy minimization approach (H^{-1} gradient flow of the Swift-Hohenberg energy on a surface) it will most likely terminate at a local minimum. However the computed minima agree with known results for V_N for $2 \leq N \leq 100$. For $N > 360$, for which grain boundary scars are expected, the computed energy in the example for $N = 492$ is only 0.001% above the lowest reported energy [4]. For large N we considered an example with $N = 99602$. The computed Coulomb energy is less than 0.0004% above the lower bound in [47] All these demonstrate the quality of the results obtained by using the phase-field-crystal model to find optimal ordering on a sphere.

Appendix A. Asymptotic analysis.

We now provide a matched asymptotic analysis to show the formal convergence of (3.1) - (3.3) to (2.3) - (2.5) as $\eta \to 0$.

A.1. New coordinates. New coordinates are established in a neighborhood of the surface Γ. To this end $r = r(x;\eta)$ is defined as a signed distance of x from Γ_η. Furthermore let $\mathbf{X} : S \to \mathbb{R}^3$ be a parametric representation of Γ, where S is an oriented manifold of dimension 2. Let $s \in S$ and $\mathbf{n} = \mathbf{n}(s;\eta)$ denote the normal. Then we assume that for $0 < r^* \ll 1$ there exists a neighborhood

$$U_\eta = \{x \in \Omega : |r(x;\eta)| < r^*\}$$

of Γ_η such that one can write $x = \mathbf{X}(s;\eta) + r(x;\eta)\mathbf{n}(s;\eta)$ for $x \in U_\eta$. Now one transforms ρ, μ, ν and ϕ to the new coordinate system:

$$\begin{aligned}
\hat{\rho}(r,s;\eta) &:= \rho(\mathbf{X}(s;\eta) + r\mathbf{n}(s;\eta);\eta), \qquad x \in U_\eta,\\
\hat{\mu}(r,s;\eta) &:= \mu(\mathbf{X}(s;\eta) + r\mathbf{n}(s;\eta);\eta), \qquad x \in U_\eta,\\
\hat{\nu}(r,s;\eta) &:= \nu(\mathbf{X}(s;\eta) + r\mathbf{n}(s;\eta);\eta), \qquad x \in U_\eta,\\
\hat{\phi}(r,s;\eta) &:= \phi(\mathbf{X}(s;\eta) + r\mathbf{n}(s;\eta);\eta), \qquad x \in U_\eta.
\end{aligned}$$

Furthermore a stretched variable is introduced $z := \frac{r}{\eta}$, and one defines

$$\begin{aligned}
R(z,s;\eta) &:= \hat{\rho}(r,s;\eta),\\
M(z,s;\eta) &:= \hat{\mu}(r,s;\eta),\\
N(z,s;\eta) &:= \hat{\nu}(r,s;\eta),\\
\Phi(z,s;\eta) &:= \hat{\phi}(r,s;\eta).
\end{aligned}$$

In addition the following Taylor expansion approximations for small η are assumed to be valid

$$\rho(x;\eta) = \rho_0(x) + \eta\rho_1(x) + \dots, \tag{A.1}$$
$$\hat{\rho}(r,s;\eta) = \hat{\rho}_0(r,s) + \eta\hat{\rho}_1(r,s) + \dots, \tag{A.2}$$
$$R(z,s;\eta) = R_0(z,s) + \eta R_1(z,s) + \dots, \tag{A.3}$$
$$\mu(x;\eta) = \mu_0(x) + \eta\mu_1(x) + \dots, \tag{A.4}$$
$$\hat{\mu}(r,s;\eta) = \hat{\mu}_0(r,s) + \eta\hat{\mu}_1(r,s) + \dots, \tag{A.5}$$
$$M(z,s;\eta) = M_0(z,s) + \eta M_1(z,s) + \dots, \tag{A.6}$$
$$\nu(x;\eta) = \nu_0(x) + \eta\nu_1(x) + \dots, \tag{A.7}$$
$$\hat{\nu}(r,s;\eta) = \hat{\nu}_0(r,s) + \eta\hat{\nu}_1(r,s) + \dots, \tag{A.8}$$
$$N(z,s;\eta) = N_0(z,s) + \eta N_1(z,s) + \dots, \tag{A.9}$$
$$\phi(x;\eta) = \phi_0(x) + \eta\phi_1(x) + \dots, \tag{A.10}$$
$$\hat{\phi}(r,s;\eta) = \hat{\phi}_0(r,s) + \eta\hat{\phi}_1(r,s) + \dots, \tag{A.11}$$
$$\Phi(z,s;\eta) = \Phi_0(z,s) + \eta\Phi_1(z,s) + \dots, \tag{A.12}$$

for which (A.1), (A.2), (A.4), (A.5), (A.7), (A.8) and (A.10), (A.11) are called outer expansions while (A.3), (A.6), (A.9) and (A.12) are called inner expansion. It is assumed that these hold simultaneously in some overlapping region and represent the same functions, which yields the matching conditions

$$\lim_{r\to\pm 0} \hat{\rho}_0(r,s,t) = \lim_{z\to\pm\infty} R_0(z,s,t), \tag{A.13}$$
$$\lim_{r\to\pm 0} \hat{\mu}_0(r,s,t) = \lim_{z\to\pm\infty} M_0(z,s,t), \tag{A.14}$$
$$\lim_{r\to\pm 0} \hat{\nu}_0(r,s,t) = \lim_{z\to\pm\infty} N_0(z,s,t), \tag{A.15}$$
$$\lim_{r\to\pm 0} \hat{\phi}_0(r,s,t) = \lim_{z\to\pm\infty} \Phi_0(z,s,t). \tag{A.16}$$

Let $H = H(s;\eta) = \frac{1}{d-1}\sum_{i=1}^{d-1}\kappa_i$ denote the mean curvature of Γ with the principal curvatures κ_i. The transform of the derivatives into the new coordinates (z,s) lead

$$\begin{aligned}\nabla u &= \eta^{-1}\partial_z U\mathbf{n} + \sum_{i,j=1}^{2} g^{ij}\partial_{s_i}U\partial_{s_j}\mathbf{X} + \mathcal{O}(\eta)\\ \Delta u &= \eta^{-2}\partial_z^2 U + \eta^{-1}H\partial_z U + \Delta_\Gamma U + \mathcal{O}(\eta),\end{aligned}$$

where $g_{ij} := \phi_{s_i}\cdot\phi_{s_j}$ and $(g^{ij}) := (g_{ij})^{-1}$. We will need the formula

$$\nabla\cdot(B(\phi)\nabla u) = \eta^{-2}\partial_z(B(\Phi)\partial_z U) + \eta^{-1}B(\Phi)H\partial_z U + B(\Phi)\Delta_\Gamma U + \mathcal{O}(\eta).$$

Because the surface Γ is fixed, we have the time derivative

$$\partial_t u = \partial_t U.$$

A.2. Outer expansion. By assumption we have $\phi_0 = 1$ in Ω_{in} and $\phi_0 = 0$ in Ω_{out} and therefore $\lim_{z\to+\infty}\Phi_0 = \lim_{r\to+0}\phi_0 = 0$ as well as $\lim_{z\to-\infty}\Phi_0 = \lim_{r\to-0}\phi_0 = 1$.

A.3. Inner expansion. Using the inner expansion in (3.1) - (3.3) we obtain in $\mathcal{O}(\eta^{-2})$

$$\begin{aligned}\partial_z(B(\Phi_0)\partial_z M_0) &= 0\\ 2\partial_z(B(\Phi_0)\partial_z R_0) + \partial_z(B(\Phi_0)\partial_z N_0) &= 0\\ \partial_z(B(\Phi_0)\partial_z R_0) &= 0\end{aligned}$$

which yields $\partial_z R_0 = 0$, $\partial_z M_0 = 0$ and $\partial_z N_0 = 0$. From this one gets $\mathcal{O}(\eta^{-1})$

$$\begin{aligned}\partial_z(B(\Phi_0)\partial_z M_1) &= 0\\ 2\partial_z(B(\Phi_0)\partial_z R_1) + \partial_z(B(\Phi_0)\partial_z N_1) &= 0\\ \partial_z(B(\Phi_0)\partial_z R_1) &= 0\end{aligned}$$

and therefore $\partial_z R_1 = 0$, $\partial_z M_1 = 0$ and $\partial_z N_1 = 0$. Finally we have in $\mathcal{O}(\eta^0)$

$$\begin{aligned}B(\Phi_0)\partial_t R_0 &= \partial_z(B(\Phi_0)\partial_z M_2) + B(\Phi_0)\Delta_\Gamma M_0,\\ B(\Phi_0)M_0 &= 2\partial_z(B(\Phi_0)\partial_z R_2) + 2B(\Phi_0)\Delta_\Gamma R_0\\ &\quad +\partial_z(B(\Phi_0)\partial_z N_2) + B(\Phi_0)\Delta_\Gamma N_0 + f'(R_0),\\ B(\Phi_0)N_0 &= \partial_z(B(\Phi_0)\partial_z R_2) + B(\Phi_0)\Delta_\Gamma R_0.\end{aligned}$$

Integration of the three equations yields

$$\begin{aligned}\partial_t R_0\int_{-\infty}^{+\infty} B(\Phi_0)\,\mathrm{d}z &= \Delta_\Gamma M_0\int_{-\infty}^{+\infty} B(\Phi_0)\,\mathrm{d}z,\\ M_0\int_{-\infty}^{+\infty} B(\Phi_0)\,\mathrm{d}z &= 2\Delta_\Gamma R_0\int_{-\infty}^{+\infty} B(\Phi_0)\,\mathrm{d}z + \Delta_\Gamma N_0\int_{-\infty}^{+\infty} B(\Phi_0)\,\mathrm{d}z\\ &\quad +f'(R_0)\int_{-\infty}^{+\infty} B(\phi_0)\,\mathrm{d}z,\\ N_0\int_{-\infty}^{+\infty} B(\Phi_0)\,\mathrm{d}z &= \Delta_\Gamma R_0\int_{-\infty}^{+\infty} B(\Phi_0)\,\mathrm{d}z.\end{aligned}$$

Dividing these equations by $\int_{-\infty}^{+\infty} B(\Phi_0)\,\mathrm{d}z$ we end up with

$$\begin{aligned}\partial_t R_0 &= \Delta_\Gamma M_0,\\ M_0 &= 2\Delta_\Gamma R_0 + \Delta_\Gamma N_0 + f'(R_0),\\ N_0 &= \Delta_\Gamma R_0\end{aligned}$$

on Γ, which lead by using the matching conditions (A.13) - (A.16) the desired equations (2.3) - (2.5).

REFERENCES

[1] S. Smale. Mathematical problems for the next century. *Math. Intelligencer*, 20:7–15, 1998.

[2] M. Shub and S. Smale. Complexity of bezout's theorem, iii: condition number and packing. *J. of Complexity*, 9:4–14, 1993.

[3] J.J. Thomson. On the structure of the atom: an investigation of the stability and periods of oscillation of a number of corpuscles arranged at equal intervals around the circumference of a circle; with application of the results on the theory of atomic structure. *Philos. Mag.*, 7:237–265, 1904.

[4] T. Erber and G.M. Hockney. Equilibrium configurations of n equal charges on a sphere. *J. Phys. A*, 24:L1369–L1377, 1991.

[5] A.R. Bausch, M.J. Bowick, A. Cacciuto, A.D. Dinsmore, M.F. Hsu, D.R. Nelson, M.G. Nikolaides, A. Travesset, and D.A. Weitz. Grain boundary scars and spherical crystallography. *Science*, 299:1716–1718, 2003.

[6] L. Ramos, T.C. Lubensky, N. Dan, P. Nelson, and D.A. Weitz. Surfactant-mediated two-dimensional crystallization of colloidal crystals. *Science*, 286:2325–2328, 1999.

[7] A.D. Dinsmore, M.F. Hsu, M.G. Nikolaides, M. Marquez amd A.R. Bausch, and D.A. Weitz. Colloidosomes: selectively permeable capsules composed of colloidal particles. *Science*, 298:1006–1009, 2002.

[8] K. Stratford, R. Adhikari, I. Pagonabarraga, J.C. Desplat, and M.E. Cates. Colloidal jamming at interfaces: a route to fluid-bicontinuous gels. *Science*, 309:2198–2201, 2005.

[9] Y.G. Sun, W.M. Choi, H.Q. Jiang, Y.Y. Huang, and J.A. Rogers. Controlled buckling of semiconductor nanoribbons for strechable electronics. *Nat. Nanotechnology*, 1:201–207, 2007.

[10] J. Lindmar, L. Mirny, and D.R. Nelson. Virus shapes and buckling transitions in spherical shells. *Phys. Rev. E*, 68:051910, 2003.

[11] R. Zandi, D. Reguera, R.F. Bruisma, W.M. Gelbart, and J. Rudnick. Origin of icosahedral symmetry in viruses. *Proc. Nat. Acad. Sci.*, 101:15556–15560, 2004.

[12] R. Zandi and D. Reguera. Mechnical properties of viral capsids. *Phys. Rev. E*, 72:021917, 2005.

[13] M.J. Bowick and L. Giomi. Two-dimensional matter: order, curvature and defects. *Adv. Phys.*, 58:449–563, 2009.

[14] S. van Teefelen, R. Backofen, A. Voigt, and H. Löwen. Derivation of the phase-field-crystal model for colloidal solidification. *Phys. Rev. E*, 79:051404, 2009.

[15] U.M.B. Marconi and P. Tarazona. Dynamic density functional theory of fluids. *J. Chem. Phys.*, 110:8032–8044, 1999.

[16] A.J. Archer and R. Evans. Dynamic density functional theory and its application to spinodal decomposition. *J. Chem. Phys.*, 121:4246–4254, 2004.

[17] T.V. Ramakrishnan and M. Yussouff. 1st-principles order-parameter theory of freezing. *Phys. Rev. B*, 19:2775–2794, 1979.

[18] K.R. Elder, N. Provatas, J. Berry, P. Stefanovic, and M. Grant. Phase-field crystal modeling and classical density functional theory of freezing. *Phys. Rev. B*, 75:064107, 2007.

[19] K.R. Elder, M. Katakowski, M. Haataja, and M. Grant. Modeling elasticity in crystal growth. *Phys. Rev. Lett.*, 88:245701, 2002.

[20] K.A. Wu and A. Karma. Phase-field crystal modeling of equilibrium bcc-liquid interfaces. *Phys. Rev. B*, 88:245701, 2007.

[21] A. Jaatinen, C.V. Achim, K.R. Elder, and T. Ala-Nissila. Thermodynamics of bcc metals n phase-field-crystal models. *Phys. Rev. E*, 80:031602, 2009.

[22] R. Backofen, A. Voigt, and T. Witkowski. Particles on curved surfaces: A dynamic approach by a phase-field-crystal model. *Phys. Rev. E*, 81:025701(R), 2010.

[23] T. Erber and G.M. Hockney. Complex systems: Equilibrium configurations of n equal charges on a sphere ($2 <= n <= 112$). *Adv. Chem. Phys.*, 98:495–594, 1997.

[24] C.M. Elliott and G. Dziuk. Finite elements on evolving surfaces. *IMA J. Num. Anal.*, 27:262–292, 2007.
[25] S. Vey and A. Voigt. Amdis - adaptive multidimensional simulations. *Comput. Vis. Sci.*, 10:57–66, 2007.
[26] D.A. Calthoun, C. Helzel, and R.J. LeVeque. Logically rectangular grids and finite volume methods for PDEs in circular and spherical domains. *SIAM Review*, 50:723–752, 2008.
[27] M. Bertalmio, L.T. Cheng, S. Osher, and G. Sapiro. Variational problems and partial differential equations on implicit surfaces. *J. Comput. Phys.*, 174:759–780, 2001.
[28] A. Rätz and A. Voigt. PDE's on surfaces - a diffuse interface approach. *Comm. Math. Sci.*, 4:575–590, 2006.
[29] A. Rätz and A. Voigt. A diffuse-interface approximation for surface diffusion including adatoms. *Nonlin.*, 20:177–192, 2007.
[30] J. Lowengrub, A. Rätz, and A. Voigt. Phase-field approximation of the dynamics of multicomponent vesicles: spinodal decomposition, coarsening, budding, and fission. *Phys. Rev. E*, 79:031926, 2009.
[31] K.E. Teigen, X. Li, J. Lowengrub, F. Wang, and A. Voigt. A diffuse-interface approach for modelling transport, diffusion and adsorption/desorption of material quantities on a deformable interface. *Comm. Math. Sci.*, 7:1009–1037, 2009.
[32] P. Schwartz, D. Adalsteinsson, P. Coletta, A.P. Arkin, and M. Onsum. Numerical computation of diffusion on a sphere. *Proc. Nat. Acad. Sci.*, 102:11151–11156, 2005.
[33] S.J. Ruuth and B. Merriman. A simple embedding method for solving partial differential equations on surfaces. *J. Comput. Phys.*, 227:2118–2129, 2008.
[34] C.M. Elliott and B. Stinner. Analysis of a diffuse interface approach to an advection diffusion equation on a moving surface. *Math. Mod. Meth. Appl. Sci.*, 19:787–802, 2009.
[35] C. Landsberg and A. Voigt. A multigrid finite element method for reaction-diffusion systems on surfaces. *Comput. Vis. Sci.*, to appear.
[36] A. Voigt and T. Witkowski. Hybrid parallelization of an adaptive finite element code. *Kybernetika*, to appear.
[37] R. Backofen, A. Rätz, and A. Voigt. Nucleation and growth by a phase-field-crystal (pfc) model. *Phil. Mag. Lett.*, 87:813–820, 2007.
[38] J. P. Boyd. *Chebyshev and Fourier Spectral Methods*. Dover Press, New York, NY, USA, second edition, 2000.
[39] J. S. Hesthaven, S. Gottlieb, and D. Gottlieb. *Spectral methods for time-dependent problems*. Cambridge Monographs on Applied and Computational Mathematics. Cambridge University Press, Cambridge, 2007.
[40] C. Müller. *Spherical Harmonics*. Springer, Aachen, 1966.
[41] L. Q. Chen and J. Shen. Applications of semi-implicit Fourier-spectral method to phase field equations. *Comput. Phys. Comm.*, 108:147–158, 1998.
[42] S. Kunis and D. Potts. Fast spherical Fourier algorithms. *J. Comput. Appl. Math.*, 161:75 – 98, 2003.
[43] J. Keiner, S. Kunis, and D. Potts. Using NFFT3 - a software library for various nonequispaced fast Fourier transforms. *ACM Trans. Math. Software*, 36:Article 19, 1 – 30, 2009.
[44] J. Keiner and D. Potts. Fast evaluation of quadrature formulae on the sphere. *Math. Comput.*, 77:397 – 419, 2008.
[45] M. Gräf, S. Kunis, and D. Potts. On the computation of nonnegative quadrature weights on the sphere. *Appl. Comput. Harmon. Anal.*, 27:124 – 132, 2009.
[46] W. Freeden, T. Gervens, and M. Schreiner. *Constructive Approximation on the Sphere*. Oxford University Press, Oxford, 1998.
[47] A. B. J. Kuijlaars and E. B. Saff. Asymptotics for minimal discrete energy on the sphere. *Trans. Amer. Math. Soc.*, 350:523–538, 1998.
[48] M. J. Bowick, D. R. Nelson, and A. Travesset. Interacting topological defects on frozen topographies. *Phys. Rev. B*, 62:8738–8751, 2000.
[49] K. Deckelnick, G. Dziuk, and C.M. Elliott. Computation of geometric partial differential equations and mean curvature flow. *Acta Numerica*, 14:139–232, 2005.
[50] B. Li, J. Lowengrub, A. Rätz, and A. Voigt. Geometric evolution laws for thin crystalline films: modelling and numerics. *Comm. Comput. Phys.*, 6:433–482, 2009.